(Preprint) AAS 19-849

SENSOR CONFIGURATION TRADE STUDY FOR NAVIGATION IN NEAR RECTILINEAR HALO ORBITS

Sehyun Yun[*], Kirsten Tuggle[†], Renato Zanetti[‡], and Chris D'Souza [§]

Deep Space Gateway is a NASA program planned to support deep-space human exploration and prove new technologies needed to achieve it. One of the Gateway requirements is to operate in the absence of communications with the Deep Space Network (DSN) for a period of at least 3 weeks. In this paper three types of onboard sensors (a camera for optical navigation, a GPS receiver, and X-ray navigation), are considered to enhance its autonomy and reduce the reliance on DSN. A trade study is conducted to explore alternatives on how to achieve autonomy and how to reduce DSN dependency while satisfying navigation performance requirements. Using linear covariance analysis, the performance of a navigation system using DSN and/or the other sensors is shown.

INTRODUCTION

NASA's Gateway is planned to be a fundamental step in returning to the moon and embarking on crewed missions beyond the Earth-moon system. The Gateway is meant to be a spaceport and center for research in order to support a human presence on the moon and prove new technologies for deep space exploration. Due to a number of favorable properties, a near rectilinear halo orbit (NRHO)[1] has been selected for the Gateway's traectory. As components such as a habitat and other modules are delivered, the Gateway will traverse its baseline NRHO in both crewed and uncrewed scenarios. It has been assumed that the primary resource for tracking and determining the Gateway's orbit at all times will be the Deep Space Network (DSN).[2] Recent work[3] has assessed the extent to which the DSN should be utilized to meet the tracking requirements for orbit determination, in both crewed and uncrewed situations. In the uncrewed case, the DSN was assumed to be the only observation source. The current work is a trade study to reduce dependency on DSN by replacing some or all DSN passes with different types of onboard measurements.

An NRHO Gateway reference trajectory has been provided[3] externally for the study. Little thrusting is expected in the uncrewed scenario beyond small orbit maintenance maneuvers. This is in contrast to the crewed scenario where potentially large forces will be exerted due to increase in venting and operations. The work begins by identifying all sensor types that can be reasonably expected for use on Gateway. Of course since the objective is orbit determination, these sensors must produce

[*]Ph.D. Student, Department of Aerospace Engineering and Engineering Mechanics, The University of Texas at Austin, Austin, TX 78712.

[†]Ph.D. Candidate, Department of Aerospace Engineering and Engineering Mechanics, The University of Texas at Austin, Austin, TX 78712.

[‡]Assistant Professor, Department of Aerospace Engineering and Engineering Mechanics, The University of Texas at Austin, Austin, TX 78712.

[§]GN&C Autonomous Flight Systems Engineer, Aeroscience and Flight Mechanics Division, NASA Johnson Space Center EG6, 2101 NASA Parkway, Houston, Texas, 77058. chris.dsouza@nasa.gov

indirect or direct observations of inertial position and velocity. Attitude determination will still be necessary, even in the uncrewed scenario, since Gateway is meant to maintain a solar pressure equilibrium attitude (SPEA). That, however, is irrelevant to the current problem since DSN provides no attitude information. For each option in the trade space, the number of DSN passes required to meet orbit determination requirements is characterized. The sensing options selected are: a camera for optical navigation, GPS, and X-ray navigation.[4] The optical camera option here specifically indicates processing of centroid and apparent diameter measurements in order to reflect use of existing Orion optical navigation algorithms.[5] The increased size of Gateway, compared to say the Orion spacecraft, opens up the possibility for accommodating a high-gain antenna for GPS signals.

A number of recent contributions exist that explore potential advantages of different onboard sensors for vehicles in a Gateway-like orbit.[1,6–10] Ref. 1 explores navigation improvements to the crewed scenario using only optical navigation processing centroid and apparent diameter measurements. Ref. 6 provides performance results when optical feature tracking is used in concert with DSN passes. New navigation packages DPS-Navigator and CAPS are developed and examined in Refs. 6 and 8, respectively. Ref. 9 offers feasible navigation performance using GNSS signals at lunar NRHO distances from Earth. Since the aim of this paper was viable of the concept in general, it did not include trades on DSN passes. Ref. 10 is most similar to the current work. There, navigation performance was examined for the sensing options of lunar beacons, X-ray pulsar navigation, and optical navigation using centroids and apparent diameters. However, since autonomy was a chief goal in that work, performance was evaluated in the context of avoiding DSN altogether. This work seeks to precisely characterize how utilizing different sensor types can alleviate the load of DSN, with the ultimate goals of more efficiently managing DSN resources. Trade options will be provided for different levels of DSN reliance (including complete autonomy), and the study will be contained to sensors which only require modest additions to Orion hardware and software.

MODELS

States

The state vector utilized is:

$$\boldsymbol{x} = \begin{bmatrix} \boldsymbol{r}^I_{GW/M} \\ \boldsymbol{v}^I_{GW/M} \end{bmatrix} \tag{1}$$

where $\boldsymbol{r}^I_{GW/M}$ and $\boldsymbol{v}^I_{GW/M}$ respectively represent the position and velocity of the Gateway spacecraft with respect to the center of the Moon in inertial coordinates (J2000).

The provided nominal trajectory is one that is currently baselined for Gateway about the Earth-Moon L2 point.[6] It is a member of a class of orbits known as Near Rectilinear Halo Orbits (NRHOs). In the Earth-Moon rotating frame, the orbit is quasi-periodic in a 9:2 resonance with the lunar synodic period, yielding an orbital period of approximately 6.5 days. Since the orbit is slowly unstable, small stationkeeping maneuvers are applied, generally at apolune. Apolune and perilune radii for the trajectory are approximately 70,000 km and 3200 km, respectively. Figure 1 shows nominal positions of Gateway with respect to the Moon in the Earth-Moon rotating frame over the course of about 1 month.

A navigation simulation can be performed by implementing a Kalman filter acting on the system for $\boldsymbol{x}$ after linearization about the nominal trajectory, $\bar{\boldsymbol{x}}$. In particular, we will examine the first-order evolution of the error covariance associated with this estimator over time and measurement updates for different candidate sensor systems.

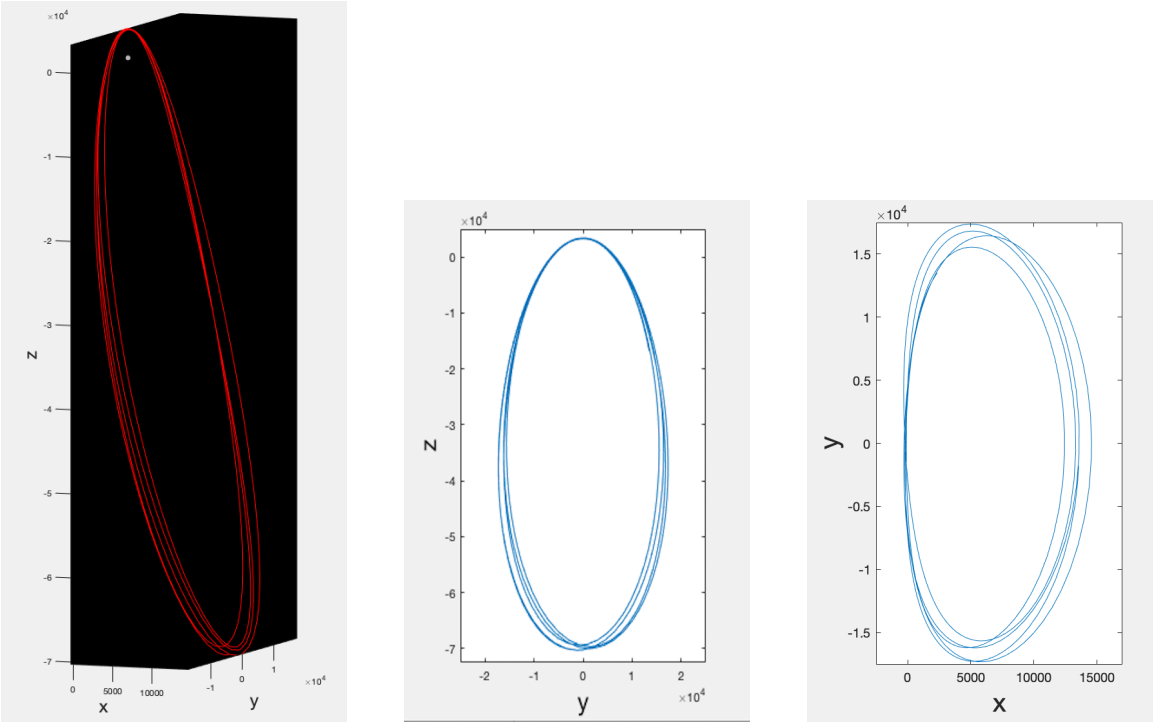

(a) 3-D Trajectory (b) 2-D Trajectory, z vs. y (c) 2-D Trajectory, y vs. x

Figure 1: Nominal Position Trajectory in Earth-Moon Rotating Frame, km

We denote deviations of the true state from the nominal as $\boldsymbol{\delta x} = \boldsymbol{x} - \bar{\boldsymbol{x}}$ and of the estimated state from the nominal as $\boldsymbol{\delta \hat{x}} = \hat{\boldsymbol{x}} - \bar{\boldsymbol{x}}$. The difference in how the true and estimated states deviate from the nominal is $\boldsymbol{e} = \boldsymbol{\delta x} - \boldsymbol{\delta \hat{x}}$. The estimation error and its covariance are then:

$$\boldsymbol{e} = \boldsymbol{x} - \hat{\boldsymbol{x}} = \boldsymbol{x} - \bar{\boldsymbol{x}} - (\hat{\boldsymbol{x}} - \bar{\boldsymbol{x}}) = \boldsymbol{\delta x} - \boldsymbol{\delta \hat{x}} = \boldsymbol{\delta e} \tag{2}$$

$$P = \mathbb{E}\{\boldsymbol{e}\boldsymbol{e}^T\} = \mathbb{E}\{\boldsymbol{\delta e}\boldsymbol{\delta e}^T\} \tag{3}$$

Note that the filter error covariances do not depend on the actual filter estimates and rather only the nominal states. This is a result of the choice to use a Kalman filter linearized about the provided nominal trajectory rather than an extended Kalman filter.

Initial Uncertainties and Navigation Requirements

The filter uncertainty is initialized using the orbital insertion error statistics below:

	3-σ Initial RSS Value
Position	20 km
Velocity	20 cm/s

with initial cross-correlations of 0 for and between position and velocity. These values, from Ref. 7, correspond to orbital insertion errors at apolune (where our nominal trajectory begins). Navigation performance requirements are to achieve 3-σ RSS values of 10 km and 10 cm/s for position and velocity, respectively.[3]

Deterministic Dynamics

The filter dynamics directly incorporate gravitational accelerations due to the Earth, Moon, and Sun. The Earth and Sun are treated as point masses or equivalently as spheres with radially symmetric density

$$\begin{aligned}\begin{bmatrix}\dot{\boldsymbol{r}}^I_{GW/M}\\ \dot{\boldsymbol{v}}^I_{GW/M}\end{bmatrix} &= \boldsymbol{f}(\boldsymbol{x},t)\\ &= \begin{bmatrix}\boldsymbol{v}^I_{GW/M}\\ \boldsymbol{a}^I_{GW/I}-\boldsymbol{a}^I_{M/I}\end{bmatrix}\\ &= \begin{bmatrix}\boldsymbol{v}^I_{GW/M}\\ -\frac{\mu_E}{\|\boldsymbol{r}^I_{GW/E}\|^3}\boldsymbol{r}^I_{GW/E}-\frac{\mu_S}{\|\boldsymbol{r}^I_{GW/S}\|^3}\boldsymbol{r}^I_{GW/S}-\frac{\mu_M}{\|\boldsymbol{r}^I_{GW/M}\|^3}\boldsymbol{r}^I_{GW/M}-\boldsymbol{a}^I_{M/I}\end{bmatrix}\end{aligned} \tag{4}$$

Since this linearized filter operates on a predefined nominal trajectory and the task at hand is one of linear covariance analysis, these dynamics are not used directly. Rather, the associated dynamics Jacobian is used to govern evolution of uncertainty.

$$F(\bar{\boldsymbol{x}},t)=\begin{bmatrix}0_{3\times3} & \mathrm{I}_3\\ G_M(\bar{\boldsymbol{r}}^I_{GW/M})+G_E(\bar{\boldsymbol{r}}^I_{GW/E})+G_S(\bar{\boldsymbol{r}}^I_{GW/S}) & 0_{3\times3}\end{bmatrix} \tag{5}$$

where

$$\begin{aligned}G_M(\bar{\boldsymbol{r}}^I_{GW/M}) &= \mu_M\left(3\frac{[\bar{\boldsymbol{r}}^I_{GW/M}][\bar{\boldsymbol{r}}^I_{GW/M}]^T}{\|\bar{\boldsymbol{r}}^I_{GW/M}\|^5}-\frac{1}{\|\bar{\boldsymbol{r}}^I_{GW/M}\|^3}\mathrm{I}_3\right)\\ G_E(\bar{\boldsymbol{r}}^I_{GW/E}) &= \mu_E\left(3\frac{[\bar{\boldsymbol{r}}^I_{GW/E}][\bar{\boldsymbol{r}}^I_{GW/E}]^T}{\|\bar{\boldsymbol{r}}^I_{GW/E}\|^5}-\frac{1}{\|\bar{\boldsymbol{r}}^I_{GW/E}\|^3}\mathrm{I}_3\right)\\ G_S(\bar{\boldsymbol{r}}^I_{GW/S}) &= \mu_S\left(3\frac{[\bar{\boldsymbol{r}}^I_{GW/S}][\bar{\boldsymbol{r}}^I_{GW/S}]^T}{\|\bar{\boldsymbol{r}}^I_{GW/S}\|^5}-\frac{1}{\|\bar{\boldsymbol{r}}^I_{GW/S}\|^3}\mathrm{I}_3\right)\end{aligned} \tag{6}$$

and

$$\begin{aligned}\bar{\boldsymbol{r}}^I_{GW/E} &= \bar{\boldsymbol{r}}^I_{GW/M}-\boldsymbol{r}^I_{E/M}\\ \bar{\boldsymbol{r}}^I_{GW/S} &= \bar{\boldsymbol{r}}^I_{GW/M}-\boldsymbol{r}^I_{S/M}\end{aligned} \tag{7}$$

utilizes the ephemerides of the Earth, Moon, and Sun available in SPICE.

Uncertain Dynamics / Process Noise

The following quantities were considered sources of process noise: burn execution errors, desaturation perturbations, and solar radiation pressure (SRP). Process noise values due to burn imperfections were modeled as in Ref. 3, using 3-σ RSS values of 1.42 mm/s and 1.5% for an additive noise term and scale factor term, respectively. A 3-σ RSS value of 3 cm/s was used for desaturation perturbations.[3] For solar radiation pressure, a constant power spectral density of $Q = 5.5\times10^{-15}I_3$ $\frac{m^2}{s^3}$ was applied to velocity uncertainties over time.[10]

OBSERVATION MODELS

DSN Measurement Model

The DSN is generally utilized for deep space missions. It assists navigation of spacecraft far from Earth with range and range-rate measurements along the line of sight (LOS) from the ground radar station to the vehicle. The DSN consists of three deep space communications facilities located roughly 120° apart around the world: at Goldstone (California, USA), Madrid (Spain), and Canberra (Australia).

The range measurement is expressed as follows:

$$\boldsymbol{h}_{\text{range}} = \left\| \boldsymbol{r}^I_{GW/E} - \boldsymbol{r}^I_{GS/E} \right\| + \boldsymbol{\nu}_{\text{range}} = \left\| \boldsymbol{r}^I_{GW/M} + \boldsymbol{r}^I_{M/E} - \boldsymbol{r}^I_{GS/E} \right\| + \boldsymbol{\nu}_{\text{range}} \tag{8}$$

where $\|\cdot\|$ is a two norm of a vector, $\boldsymbol{r}^I_{GW/E}$, $\boldsymbol{r}^I_{GS/E}$, and $\boldsymbol{r}^I_{M/E}$ are the position vector of Gateway, ground station and the Moon with respect to Earth in inertial frame, respectively, and $\boldsymbol{r}^I_{GW/M}$ is the position vector of Gateway with respect to the Moon in inertial frame. Since $\boldsymbol{h}_{\text{range}}$ is invariant to the origin or orientation of the coordinate frame used, Eq. (8) provides multiple, equivalent expressions. The linear range measurement model is described as

$$\boldsymbol{H}_{\text{range}}(\bar{x})\delta\boldsymbol{x} = \frac{(\boldsymbol{r}^I_{GW/M} + \boldsymbol{r}^I_{M/E} - \boldsymbol{r}^I_{GS/E})^{\mathrm{T}}}{\left\| \boldsymbol{r}^I_{GW/M} + \boldsymbol{r}^I_{M/E} - \boldsymbol{r}^I_{GS/E} \right\|} \delta\boldsymbol{r}^I_{GW/M} \tag{9}$$

and the range measurement noise sequence is modeled as:

$$\boldsymbol{\nu}_{\text{range}} \overset{\text{i.i.d}}{\sim} N(0\ \text{m}, 1\ \text{m}^2) \tag{10}$$

where $N(\mu, \sigma^2)$ represents the Gaussian pdf with mean μ and covariance σ^2.

The range-rate measurement is obtained by differentiating Eq. (8) with respect to time.

$$\boldsymbol{h}_{\text{rangerate}} = \frac{(\boldsymbol{r}^I_{GW/M} + \boldsymbol{r}^I_{M/E} - \boldsymbol{r}^I_{GS/E})^{\mathrm{T}} (\dot{\boldsymbol{r}}^I_{GW/M} + \dot{\boldsymbol{r}}^I_{M/E} - \dot{\boldsymbol{r}}^I_{GS/E})}{\left\| \boldsymbol{r}^I_{GW/M} + \boldsymbol{r}^I_{M/E} - \boldsymbol{r}^I_{GS/E} \right\|} + \boldsymbol{\nu}_{\text{rangerate}} \tag{11}$$

where $\dot{\boldsymbol{r}}$ is the time rate of change of the position vector. The linear range-rate measurement model is express as follows:

$$\boldsymbol{H}_{\text{rangerate}}(\bar{x})\delta\boldsymbol{x} = \begin{bmatrix} \frac{\partial \boldsymbol{h}_{\text{rangerate}}}{\partial \boldsymbol{x}_{\text{pos}}} & \frac{\partial \boldsymbol{h}_{\text{rangerate}}}{\partial \boldsymbol{x}_{\text{vel}}} \end{bmatrix} \begin{bmatrix} \delta\boldsymbol{r}^I_{GW/M} \\ \delta\boldsymbol{v}^I_{GW/M} \end{bmatrix} \tag{12}$$

where

$$\begin{aligned} \frac{\partial \boldsymbol{h}_{\text{rangerate}}}{\partial \boldsymbol{x}_{\text{pos}}} =& \frac{(\dot{\boldsymbol{r}}^I_{GW/M} + \dot{\boldsymbol{r}}^I_{M/E} - \dot{\boldsymbol{r}}^I_{GS/E})^{\mathrm{T}}}{\left\| \boldsymbol{r}^I_{GW/M} + \boldsymbol{r}^I_{M/E} - \boldsymbol{r}^I_{GS/E} \right\|} \\ & \cdot \left[\mathbf{I}_{3\times 3} - \frac{(\boldsymbol{r}^I_{GW/M} + \boldsymbol{r}^I_{M/E} - \boldsymbol{r}^I_{GS/E})(\boldsymbol{r}^I_{GW/M} + \boldsymbol{r}^I_{M/E} - \boldsymbol{r}^I_{GS/E})^{\mathrm{T}}}{\left\| \boldsymbol{r}^I_{GW/M} + \boldsymbol{r}^I_{M/E} - \boldsymbol{r}^I_{GS/E} \right\|^2} \right] \end{aligned} \tag{13}$$

$$\frac{\partial \boldsymbol{h}_{\text{rangerate}}}{\partial \boldsymbol{x}_{\text{vel}}} = \frac{(\boldsymbol{r}^I_{GW/M} + \boldsymbol{r}^I_{M/E} - \boldsymbol{r}^I_{GS/E})^{\mathrm{T}}}{\left\| \boldsymbol{r}^I_{GW/M} + \boldsymbol{r}^I_{M/E} - \boldsymbol{r}^I_{GS/E} \right\|} \tag{14}$$

and the range-rate measurement noise sequence is modeled as:

$$\boldsymbol{\nu}_{\text{rangerate}} \overset{\text{i.i.d}}{\sim} N(0\ \text{mm}, 1\ \text{mm}^2) \tag{15}$$

Although accurate position and velocity can be estimated using DSN, it requires sizeable ground operation and scheduling to coordinate the observations. The measurement models for difference sensor types such as optical, GPS, and X-ray measurement are used to reduce the load of DSN for this study.

Optical Measurement Models

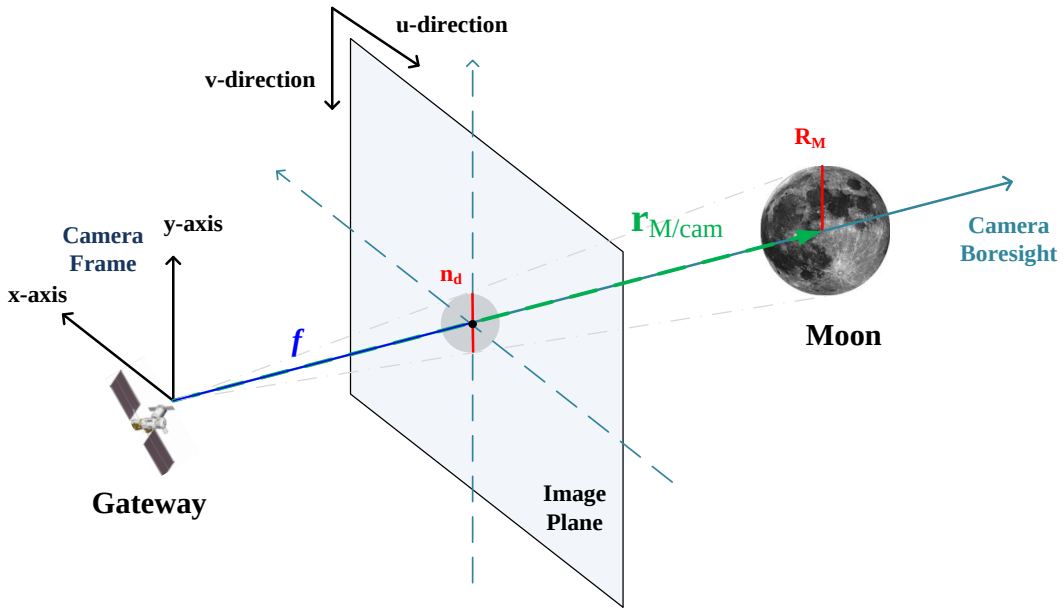

Figure 2: Concept of optical camera measurements

The centroid and apparent diameter of the Moon is measured differently depending on the observer's relative position. An optical camera can measure it using image processing algorithm. The optical camera measurement model and a linear form with respect to the states of Gateway are presented. A pin hole camera model is used for this study. Figure 2 shows the concept of optical camera measurements: the centroid and apparent diameter of the Moon.

The position vector of the Moon with respect to the camera in the camera frame is defined as follows:

$$\boldsymbol{r}^{cam}_{M/cam} = -\boldsymbol{T}^{\text{cam}}_{\text{I}}(\epsilon_{cam}) \left(\boldsymbol{r}^{I}_{GW/M} + \boldsymbol{r}^{I}_{cam/GW} \right) \tag{16}$$

where $\boldsymbol{r}^{cam}_{M/cam}$ is the position vector of the Moon with respect to the camera in the camera frame, $\boldsymbol{T}^{cam}_{I}$ is the transformation matrix from inertial coordinates to camera coordinates, ϵ_{cam} is the misalignment of the camera with respect to Gateway, and $\boldsymbol{r}^{I}_{cam/GW}$ is the position vector of the camera with respect to Gateway in inertial frame. Then, the variation of Eq. (16) is expressed as follows:

$$\delta\boldsymbol{r}^{cam}_{M/cam} = -\delta\boldsymbol{T}^{\text{cam}}_{\text{I}}(\epsilon_{cam}) \left(\boldsymbol{r}^{I}_{GW/M} + \boldsymbol{r}^{I}_{cam/GW} \right) - \boldsymbol{T}^{\text{cam}}_{\text{I}} \delta\boldsymbol{r}^{I}_{GW/M} - \boldsymbol{T}^{\text{cam}}_{\text{I}} \delta\boldsymbol{r}^{I}_{cam/GW} \tag{17}$$

The centroid of the Moon measurement model is derived analytically with the assumption that the camera is pointing at the Moon. Then, the variation of the pixel location with respect to the position vector of the camera in camera frame can be obtained as follows:

$$\begin{bmatrix}\delta u\\ \delta v\end{bmatrix} = -f\begin{bmatrix}\frac{s}{z^{cam}_{M/cam}} & 0 & 0\\ 0 & \frac{s}{z^{cam}_{M/cam}} & 0\end{bmatrix}\delta \boldsymbol{r}^{cam}_{M/cam} = \begin{bmatrix}\boldsymbol{c}_1\\ \boldsymbol{c}_2\end{bmatrix}\delta \boldsymbol{r}^{cam}_{M/cam} \tag{18}$$

where u and v are the camera measurements, f is the camera focal length, 35.1 mm, and s is the pixel pitch, 4.8×10^{-6} m/pixel. Then, the partials of the Moon centroid measurements are described as:

$$\frac{\partial u}{\partial \boldsymbol{r}^I_{GW/M}} = \frac{\partial u}{\partial \boldsymbol{r}^{cam}_{M/cam}}\frac{\partial \boldsymbol{r}^{cam}_{M/cam}}{\partial \boldsymbol{r}^I_{GW/M}} = -\boldsymbol{c}_1\boldsymbol{T}^{\text{cam}}_{\text{I}} \tag{19}$$

$$\frac{\partial u}{\partial \epsilon_{cam}} = \frac{\partial u}{\partial \boldsymbol{r}^{cam}_{M/cam}}\frac{\partial \boldsymbol{r}^{cam}_{M/cam}}{\partial \epsilon_{cam}} = -\boldsymbol{c}_1\boldsymbol{T}^{\text{cam}}_{\text{I}}\left[(\boldsymbol{r}^I_{GW/M}+\boldsymbol{r}^I_{cam/GW})\times\right] \tag{20}$$

$$\frac{\partial u}{\partial \boldsymbol{r}^I_{cam/GW}} = \frac{\partial u}{\partial \boldsymbol{r}^{cam}_{M/cam}}\frac{\partial \boldsymbol{r}^{cam}_{M/cam}}{\partial \boldsymbol{r}^I_{cam/GW}} = -\boldsymbol{c}_1\boldsymbol{T}^{\text{cam}}_{\text{I}} \tag{21}$$

$$\frac{\partial v}{\partial \boldsymbol{r}^I_{GW/M}} = \frac{\partial v}{\partial \boldsymbol{r}^{cam}_{M/cam}}\frac{\partial \boldsymbol{r}^{cam}_{M/cam}}{\partial \boldsymbol{r}^I_{GW/M}} = -\boldsymbol{c}_2\boldsymbol{T}^{\text{cam}}_{\text{I}} \tag{22}$$

$$\frac{\partial v}{\partial \epsilon_{cam}} = \frac{\partial v}{\partial \boldsymbol{r}^{cam}_{M/cam}}\frac{\partial \boldsymbol{r}^{cam}_{M/cam}}{\partial \epsilon_{cam}} = -\boldsymbol{c}_2\boldsymbol{T}^{\text{cam}}_{\text{I}}\left[(\boldsymbol{r}^I_{GW/M}+\boldsymbol{r}^I_{cam/GW})\times\right] \tag{23}$$

$$\frac{\partial v}{\partial \boldsymbol{r}^I_{cam/GW}} = \frac{\partial v}{\partial \boldsymbol{r}^{cam}_{M/cam}}\frac{\partial \boldsymbol{r}^{cam}_{M/cam}}{\partial \boldsymbol{r}^I_{cam/GW}} = -\boldsymbol{c}_2\boldsymbol{T}^{\text{cam}}_{\text{I}} \tag{24}$$

where

$$\left[\boldsymbol{a}\times\right] = \begin{bmatrix}0 & -a_3 & a_2\\ a_3 & 0 & -a_1\\ -a_2 & a_1 & 0\end{bmatrix} \tag{25}$$

is the skew-symmetric matrix representation of the cross product for a vector $\boldsymbol{a}$.

The apparent diameter measurement is expressed as follows:

$$n_d = \frac{2R_M f s}{\sqrt{r^2_{M/cam}-R^2_M}} \tag{26}$$

where n_d is the angular diameter of the Moon in pixels, R_M is the Moon radius, and $r_{M/cam}$ is the distance between the Moon and camera. Then, the variation of the angular diameter measurement is obtained as follows:

$$\delta n_d = \frac{r_{M/cam}n_d}{r^2_{M/cam}-R^2_M}\frac{(\boldsymbol{r}^{cam}_{M/cam})^{\text{T}}}{r_{M/cam}}\delta \boldsymbol{r}^{cam}_{M/cam} = \boldsymbol{d}\delta \boldsymbol{r}^{cam}_{M/cam} \tag{27}$$

so that the partial for the apparent diameter measurement is described as:

$$\frac{\partial n_d}{\partial \boldsymbol{r}^I_{GW/M}} = \frac{\partial n_d}{\partial \boldsymbol{r}^{cam}_{M/cam}} \frac{\partial \boldsymbol{r}^{cam}_{M/cam}}{\partial \boldsymbol{r}^I_{GW/M}} = -\boldsymbol{dT}^{\text{cam}}_{\text{I}} \tag{28}$$

$$\frac{\partial n_d}{\partial \epsilon_{cam}} = \frac{\partial n_d}{\partial \boldsymbol{r}^{cam}_{M/cam}} \frac{\partial \boldsymbol{r}^{cam}_{M/cam}}{\partial \epsilon_{cam}} = -\boldsymbol{dT}^{\text{cam}}_{\text{I}} \left[(\boldsymbol{r}^I_{GW/M} + \boldsymbol{r}^I_{cam/GW}) \times \right] \tag{29}$$

$$\frac{\partial n_d}{\partial \boldsymbol{r}^I_{cam/GW}} = \frac{\partial n_d}{\partial \boldsymbol{r}^{cam}_{M/cam}} \frac{\partial \boldsymbol{r}^{cam}_{M/cam}}{\partial \boldsymbol{r}^I_{cam/GW}} = -\boldsymbol{dT}^{\text{cam}}_{\text{I}} \tag{30}$$

The centroid and apparent diameter measurement noises are based on the one for Orion's Exploration Mission 1.[5] Measurement noise error models are expressed as follows:

$$\sigma_\alpha = \sqrt{(0.15 \text{ pix})^2 + \left(\frac{f(6562 \text{ ft}}{sr_{M/cam}} \right)^2} \tag{31}$$

$$\sigma_\beta = \sqrt{(0.06 \text{ pix})^2 + \left(\frac{f(6562 \text{ ft}}{2sr_{M/cam}} \right)^2} \tag{32}$$

$$\sigma_d = \sqrt{(0.12 \text{ pix})^2 + \left(\frac{f(6562 \text{ ft}}{sr_{M/cam}} \right)^2} \tag{33}$$

where α and β means the parallel and perpendicular axis to the Moon-Sun direction, respectively, and σ_d is the resulting diameter error in pixels. The bias models are described as:

$$b_\alpha = (0.383 \text{ pix}) - \frac{3.470 \times 10^8 \text{ pix-ft}}{r_{M/cam}} \tag{34}$$

$$b_\beta = 0 \tag{35}$$

$$b_d = (-0.236 \text{ pix}) - \frac{1.964 \times 10^8 \text{ pix-ft}}{r_{M/cam}} \tag{36}$$

The Orion camera model is used for this analysis which has a field of view of 20 $\times$ 16 degree. Moreover, the camera misalignment and camera position bias are 45 arcsec and 0.3 m, 3σ, on each axis, respectively. The measurement covariance for the camera misalignment and position bias can be obtained using Eq. (20), Eq. (21), Eq. (23), Eq. (24), Eq. (29), and Eq. (30).

GPS Measurement Models

Global positioning system (GPS) is widely used to estimate the states of a number of satellites in low Earth orbit (LEO). However, expanding GPS use into deep space such as the Geostationary Operational Environmental Satellite R (GOES-R) and the Magnetospheric Multiscale Mission (MMS) has been studied.[11–13] The two missions have shown that it is possible to receive a sidelobe or edge of the main lobe GPS signals that cross the Earth's limb. Moreover, simulations have shown that GPS use can be expanded to lunar distance with a high-gain antenna. For this study, it is assumed that high-sensitivity GPS receiver has a threshold of around 20 dB-Hz and GPS has a high-gain antenna with peak gain of 15 dB, which would be less than about 1 m in diameter.[14]

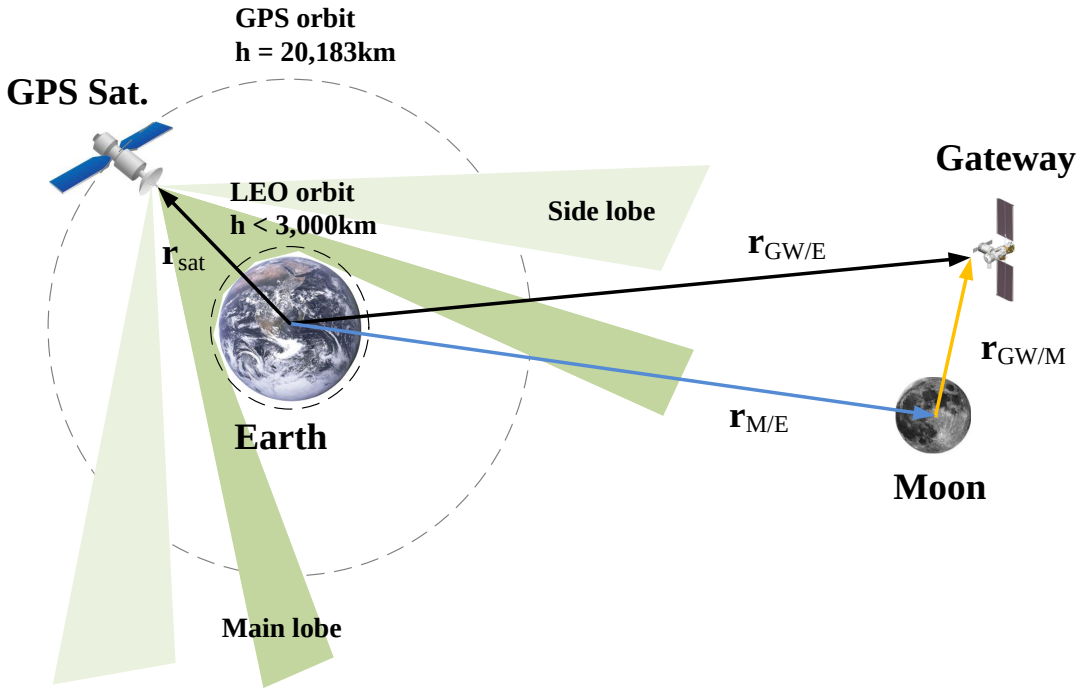

Figure 3: Concept of GPS signal use at high altitude

The pseudo-range measurement is modeled as follows:

$$\rho = \left\| \boldsymbol{r}^I_{GW/E} - \boldsymbol{r}^I_{sat/E} \right\| + \nu_\rho = \left\| \boldsymbol{r}^I_{GW/M} + \boldsymbol{r}^I_{M/E} - \boldsymbol{r}^I_{sat/E} \right\| + \nu_\rho \tag{37}$$

where $\boldsymbol{r}^I_{sat/E}$ is the position vector of the observed satellite with respect to Earth in inertial frame and v_ρ is the Gaussian measurement noise. Hence, the linear measurement model is obtained as

$$\boldsymbol{H}(\bar{x})\delta\boldsymbol{x} = \frac{(\boldsymbol{r}^I_{GW/M} + \boldsymbol{r}^I_{M/E} - \boldsymbol{r}^I_{sat/E})^{\mathrm{T}}}{\left\| \boldsymbol{r}^I_{GW/M} + \boldsymbol{r}^I_{M/E} - \boldsymbol{r}^I_{sat/E} \right\|} \delta\boldsymbol{r}^I_{GW/M} \tag{38}$$

The pseudo-range accuracy of the GPS measurement is 30 m, 3σ.[11] GPS satellites data are available based on SatNav ToolBox 2.0 for Matlab and the simulation start time is on December 26th, 2016. The ability to track sidelobes can contribute to the robustness and quality of the Gateway navigation. However, this paper only considers main lobe because the sidelobe signals have not yet been completely specified at the Moon distance. Since main lobe signals can extend out to angles of up to 47°, the line of sight vector is limited less than 23.5° from the GPS satellite's antenna boresight.[13]

X-ray Measurement Models

Since X-ray pulsars are observed over the sky map and they are of unique period and strength, X-ray pulsar navigation (XNav) has been proposed and used in a variety of studies.[15–17] For a trade study to reduce dependency from DSN, XNav is applied for this study. XNav uses periodic X-ray

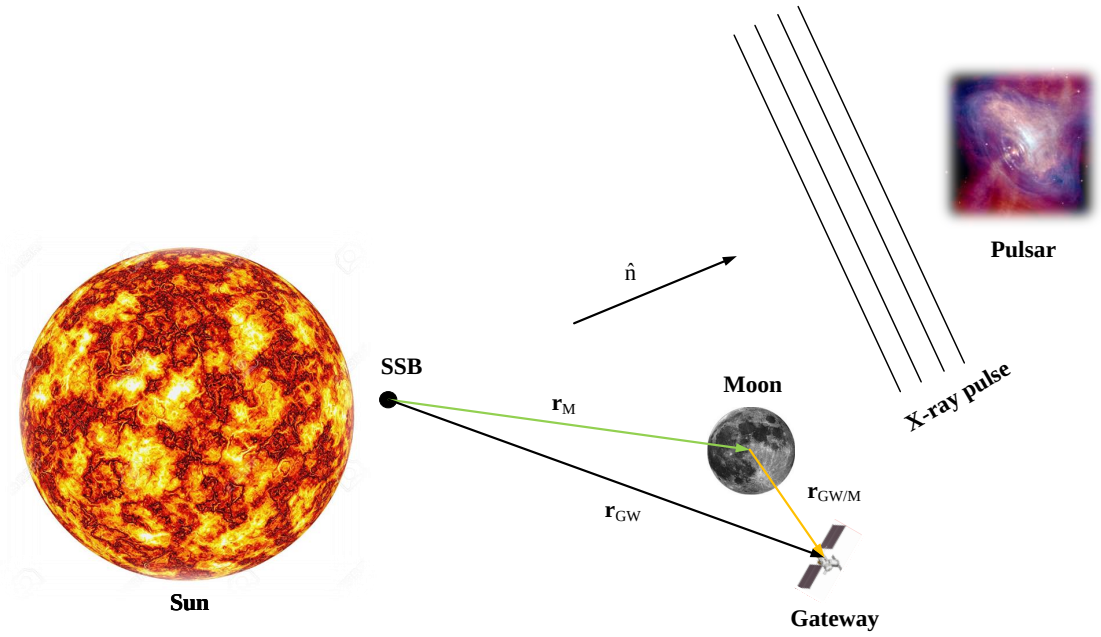

Figure 4: Concept of X-ray pulsar navigation

pulsars emitted from a set of known pulsars in order to estimate the state of Gateway in deep space. Similar to DSN or GPS, X-ray sensors are used to compute the pulsar-based range measurements by comparing measured and predicted pulse time of arrival (TOA). However, XNav does not require assistance from external navigation system.

The concept of XNav is shown in Figure 4. XNav are performed in an inertial system whose origin is the solar system barycenter (SSB). After receiving the X-ray pulse, the range measurement for Gateway to a reference point, $\boldsymbol{r}^I_{GW}$, is obtained by comparing the measured pulse TOA, t_{GW}, at the vehicle to its predicted TOA, t_{SSB}, at the reference point.

$$t_{SSB} = t_{GW} + \frac{\hat{\boldsymbol{n}}_i \cdot \boldsymbol{r}^I_{GW}}{c} + H.O.T. = t_{GW} + \frac{\hat{\boldsymbol{n}}_i}{c} \cdot (\boldsymbol{r}^I_M + \boldsymbol{r}^I_{GW/M}) + H.O.T. \tag{39}$$

where $\hat{\boldsymbol{n}}_i$ is the unit vector to the selected i^{th} pulsar, c is the speed of light, and $\boldsymbol{r}^I_M$ is the position of the Moon with respect to the SSB. Since high order terms (H.O.T.) are several orders of magnitude smaller, only the first order terms is considered in this paper. If the position is defined as follows:

$$\boldsymbol{r}^I_{GW/M} = \bar{\boldsymbol{r}}^I_{GW/M} + \delta\boldsymbol{r}^I_{GW/M} \tag{40}$$

then, Eq. (39) can be expressed in linear form with respect to $\delta\boldsymbol{r}^I_{GW/M}$ as

$$c(t_{SSB} - t_{GW}) - \hat{\boldsymbol{n}}_i \left(\boldsymbol{r}^I_M + \bar{\boldsymbol{r}}^I_{GW/M}\right) = \hat{\boldsymbol{n}}_i \cdot \delta\boldsymbol{r}^I_{GW/M} \tag{41}$$

Therefore, the linear measurement model of XNav can be constructed as

$$\boldsymbol{H}(\bar{x})\delta\boldsymbol{x} = \hat{\boldsymbol{n}}_i \cdot \delta\boldsymbol{r}^I_{GW/M} \tag{42}$$

The measurement noise is applied based on the accuracy from SEXTANT on-orbit results, which is 10 km, 3σ.[17] Tanking into account the best dilution of precision (DOP), the four pulsars, B0531+21, B0540-69, B1821-24, and B1937+21 are selected as navigation pulsars. The parameters of the pulsars are listed in Table 1.

Table 1: Characters of the candidate X-ray pulsars

Parameter	B0531+21	B0540-69	B1821-24	B1937+21
Galactic Latitude (°)	184.56	279.72	7.80	57.51
Galactic Longitude (°)	-5.78	-31.52	-5.58	-0.29
Right Ascension (°) (J2000)	83.63322	85.04667	276.13337	294.91067
Declination (°) (J2000)	22.01446	-69.33171	-24.86968	21.58309
Period (ms)	33.392	50.570	3.054	1.558

SIMULATION RESULTS

Linear covariance analysis is conducted to evaluate the capability of onboard sensors for alleviating the load of DSN. Linear covariance analysis produces the same covariance generated by Monte Carlo simulations in a single simulation by directly propagating and updating the error covariance matrix $\boldsymbol{P}$ in Eq. (3).[18] The covariance propagation and update equations are expressed as follows:

$$\boldsymbol{P}^{-}_{k|k-1} = \boldsymbol{F}_{k-1}\boldsymbol{P}^{+}_{k-1|k-1}\boldsymbol{F}^{\mathrm{T}}_{k-1} + \boldsymbol{Q}_{k-1} \tag{43}$$

$$\boldsymbol{P}^{+}_{k|k} = \boldsymbol{P}^{-}_{k|k-1} - \boldsymbol{K}_k\left(\boldsymbol{H}_k\boldsymbol{P}^{-}_{k|k-1}\boldsymbol{H}^{\mathrm{T}}_k + \boldsymbol{R}_k\right)\boldsymbol{K}^{\mathrm{T}}_k \tag{44}$$

where $\boldsymbol{P}^{-}$ and $\boldsymbol{P}^{+}$ are the a priori and a posteriori covariance matrices, respectively. $\boldsymbol{F}$ is the state transition matrix and $\boldsymbol{H}$ is the measurement matrix. $\boldsymbol{Q}$ and $\boldsymbol{R}$ are the process and measurement noise covariance matrices, respectively. The Kalman gain, $\boldsymbol{K}$, is calculated as

$$\boldsymbol{K}_k = \boldsymbol{P}^{-}_{k|k-1}\boldsymbol{H}^{\mathrm{T}}_k\left(\boldsymbol{H}_k\boldsymbol{P}^{-}_{k|k-1}\boldsymbol{H}^{\mathrm{T}}_k + \boldsymbol{R}_k\right)^{-1} \tag{45}$$

The above four measurement types are used for this simulation and the details of the measurements are as follows. DSN measurement should be used at least 3 contacts per the period, each 6-hours long, to meet the navigation performance requirements.[7] For this study, within an observation period, range and range-rate measurements are available every 5 minutes and 1 minute, respectively. OpNav provides daily measurements every 30 seconds with a pass lasting 10 minutes. In addition, measurements are also taken right before the stationkeeping burns with a longer pass lasting 2 hours. GPS measurements are assumed every 1 minute for the entire orbit. X-ray measurements are taken every 3 hours. The simulated results are shown for a duration of about five weeks.

Figure 5 shows the comparison of position and velocity navigation errors for each sensor for Gateway. The navigation errors peak at perilune when Gateway has the highest velocity. For OpNav and XNav cases, the position and velocity errors exceed the navigation requirement around perilune. In GPS navigation case, the number of observable satellites are from 0 to 3, and 0.48 satellites were observed on average. This is why the velocity error of Gateway with GPS navigation does not satisfy

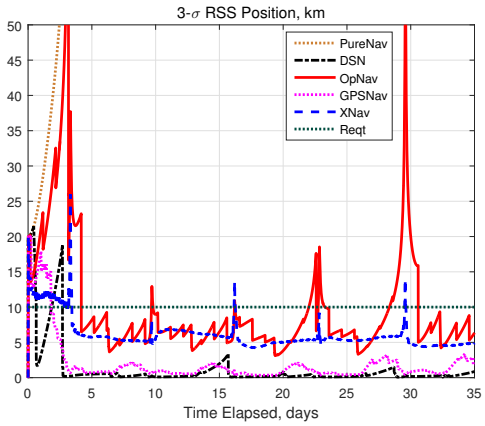

(a) Position errors

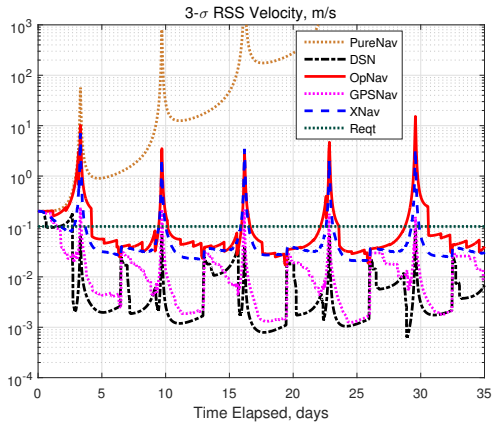

(b) Velocity errors

Figure 5: Position and velocity error of Gateway with one sensor

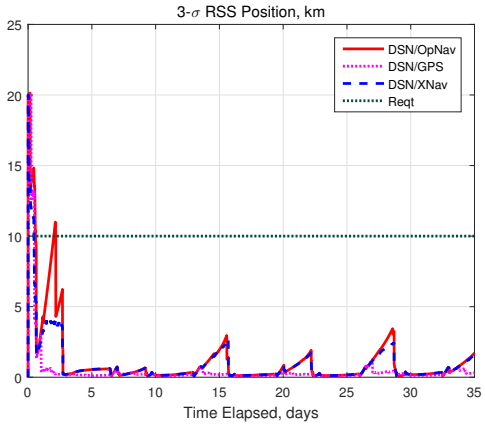

(a) Position errors

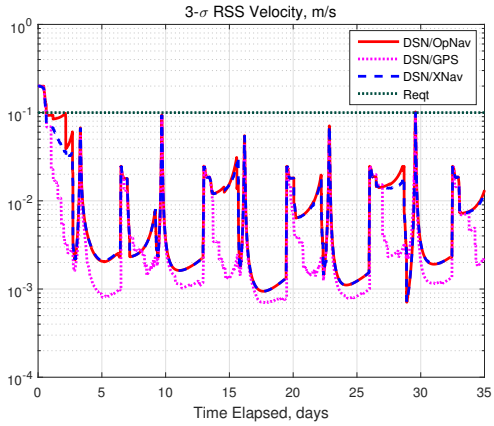

(b) Velocity errors

Figure 6: Position and velocity error of Gateway with two sensors

the requirement around perilune. On the other hand, DSN navigation satisfies the requirement over the time except for the first three days. The navigation error of the un-aided inertial system diverges.

The navigation error of Gateway with combining DSN and each sensor is shown in Figure 6. The DSN measurement time is reduced from every 6 hours to 5 hours within the observation period with OpNav and XNav. Moreover, the DSN load can be reduced to 4 hours with the help of GPS sensor. Figure 7 shows the 3-σ values of Gateway with integrating other two sensors into DSN. The navigation performance of DSN with OpNav and XNav is almost the same as that of DSN with OpNav or XNav. However, the load of DSN can be reduce by half, 3 hours, with GPS and OpNav or XNav. The navigation performance of Gateway with all sensors is depicted in Figure 8. In that case, every 2 hours DSN measurements are enough to meet the navigation requirement. The linear covariance analysis simulation results are summarized in Table 2.

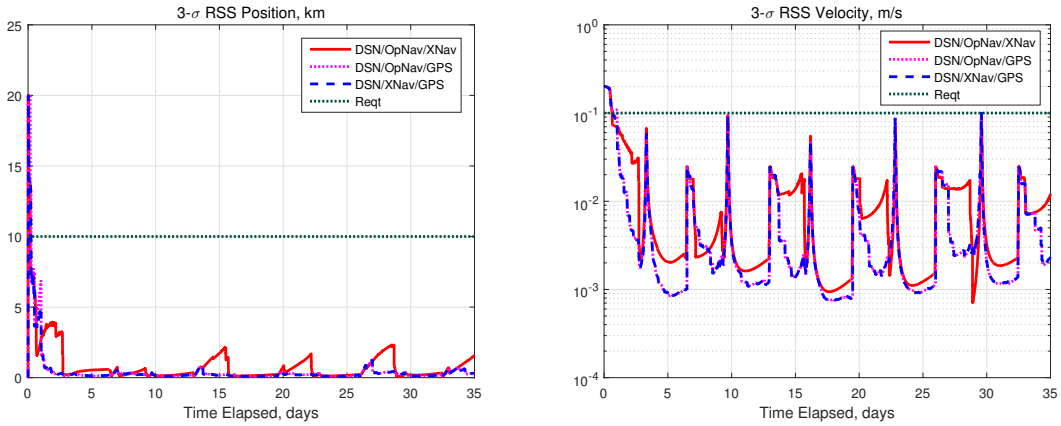

(a) Position errors (b) Velocity errors

Figure 7: Position and velocity error of Gateway with three sensors

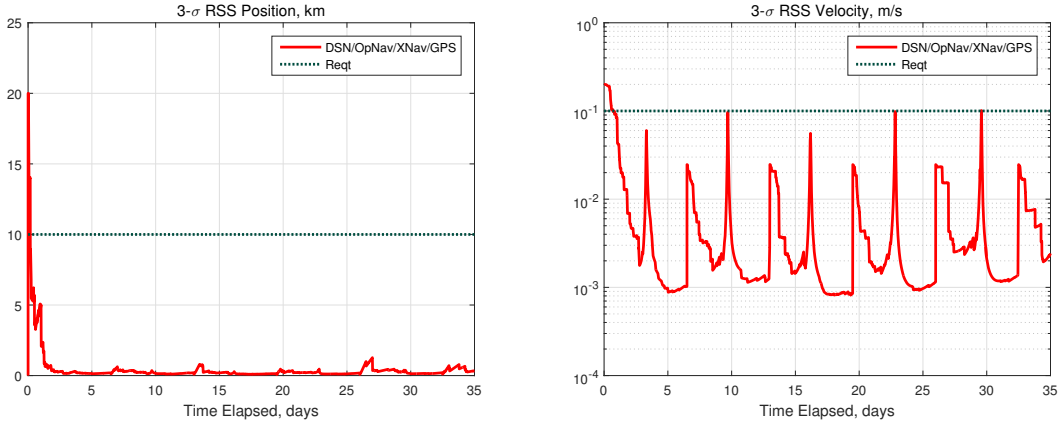

(a) Position errors (b) Velocity errors

Figure 8: Position and velocity error of Gateway with all sensors

CONCLUSIONS

In this paper, three types of onboard sensors, a camera for OpNav and an antenna for GPS and XNav, are analyzed to alleviate the load of DSN. Each measurement model for Gateway are described and linear covariance analysis is used to find the more efficient way to manage DSN resources. In the computer simulation, it is shown that Gateway with combining DSN with each sensor reduces the load of DSN. Although the navigation performance of Gateway with combining DSN with OpNav or XNav is almost the same as that of Gateway with integrating DSN into two sensors, using GPS and OpNav or XNav together alleviates the load of DSN in comparison with that of DSN with only GPS. Moreover, when all sensors are used for the orbit determination, it further reduces the dependency on DSN comparing to using DSN with other two sensors.

Table 2: The capability of onboard sensors for alleviating the load of DSN

DSN	OpNav	GPS	XNav	DSN measurement time (hrs)
o				6
o	o			5
o		o		4
o			o	5
o	o	o		3
o	o		o	5
o		o	o	3
o	o	o	o	2

REFERENCES

[1] E. M. Zimovan, K. C. Howell, and D. C. Davis, "Near Rectilinear Halo Orbits and Their Application in Cis-Lunar Space," *3rd IAA Conference on Dynamics and Control of Space Systems, Moscow, Russia*, 2017.

[2] S. E. Wolff, "Deep Space Network," 2003.

[3] W. G. Newman, Davis and Ryne, "Stationkeeping, Orbit Determination, and Attitude Control for Spacecraft in Near Rectilinear Halo Orbits," *AAS/AIAA Astrodynamics Specialist Conference*, 2018.

[4] S. I. Sheikh, D. J. Pines, P. S. Ray, K. S. Wood, M. N. Lovellette, and M. T. Wolff, "Spacecraft navigation using X-ray pulsars," *Journal of Guidance, Control, and Dynamics*, Vol. 29, No. 1, 2006, pp. 49–63.

[5] G. N. Holt, C. N. D'Souza, and D. W. Saley, "Orion Optical Navigation Progress Toward Exploration Mission 1," *2018 Space Flight Mechanics Meeting*, 2018.

[6] C. P. Newman, R. Sieling, D. C. Davis, and R. J. Whitley, "Attitude Control and Orbit Determination of a Crewed Spacecraft With a Lander in Near Rectilinear Halo Orbit," *29th AAS/AIAA Space Flight Mechanics Meeting*, AAS 19-545.

[7] J. R. Guinn, S. Bhaskaran, T. A. Ely, B. M. Kennedy, T. J. Martin-Mur, R. S. Park, J. E. Riedel, D. C. Roth, and A. T. Vaughan, "The Deep Space Positioning System (DPS) Navigator Concept for the Lunar Gateway," *42nd Annual AAS Guidance and Control Conference*, AAS 19-093.

[8] J. S. Parker, J. Smith, A. Forsman, C. Rabotin, C. Cain, and B. Cheetham, "The Cislunar Autonomous Positioning System (CAPS)," *42nd Annual AAS Guidance and Control Conference*, AAS 19-094.

[9] Y. Nakajima, T. Yamamoto, and H. Ikeda, "Using GNSS Receiver at Near Rectlinear Halo Orbit," *29th AAS/AIAA Space Flight Mechanics Meeting*, AAS 19-276.

[10] S. Bhatt, S. Steffes, and G. Barton, "A Deep Space Autonomous Navigation System for the Lunar Orbital Platform-Gateway," *42nd Annual AAS Guidance and Control Conference*, AAS 19-092.

[11] L. B. Winternitz, W. A. Bamford, S. R. Price, J. R. Carpenter, A. C. Long, and M. Farahmand, "Global Positioning System Navigation Above 76,000 KM for NASA'S Magnetospheric Multiscale Mission," *NAVIGATION: Journal of The Institute of Navigation*, Vol. 64, No. 2, 2017, pp. 289–300.

[12] B. W. Ashman, F. H. Bauer, J. J. K. Parker, and J. E. Donaldson, "GPS Operations in High Earth Orbit: Recent Experiences and Future Opportunities," *2018 SpaceOps Conference*, 2018.

[13] B. W. Ashman, J. J. K. Parker, F. H. Bauer, and M. Esswein, "Exploring the Limits of High-Altitude GPS for Future Lunar Missions," *41st Annual AAS Guidance and Control Conference*, 2018.

[14] Y. Nakajima, T. Yamamoto, and H. Ikeda, "Using GNSS Receiver at Near Rectlinear Halo Orbit," *29th AAS/AIAA Space Flight Mechanics Meeting*, 2019.

[15] S. I. Sheikh, D. J. Pines, P. S. Ray, K. S. Wood, M. N. Lovellette, and M. T. Wolff, "Spacecraft Navigation Using X-Ray Pulsars," *Journal of Guidance, Control, and Dynamics*, Vol. 29, No. 1, 2006, pp. 49–63. doi: 10.2514/1.13331.

[16] A. A. Emadzadeh and J. L. Speyer, "Navigation in Space by X-ray Pulsars," 2011. doi: 10.1007/978-1-4419-8017-5.

[17] L. B. Winternitz, M. A. Hassouneh, J. W. Mitchell, S. R. Price, W. H. Yu, S. R. Semper, P. S. Ray, K. S. Wood, Z. Arzoumanian, and K. C. Gendreau, "SEXTANT X-ray Pulsar Navigation Demonstration: Additional On-Orbit Results," *2018 SpaceOps Conference*, 2018. doi: 10.2514/6.2018-2538.

[18] P. S. Maybeck, "Stochastic Models, Estimation, and Control," 1979, pp. 325–341. ISBN: 978-0-12-411042-7.